Observational study of the type IIb supernovae 2017gkk and 2019gaf

Master's thesis
University of Turku
Astronomy
December 2022
B.Sc. Niilo Koivisto
Examiners:
Prof. Seppo Mattila
Docent Hanindyo Kuncarayakti
Supervisors:
Dr. Takashi Nagao
Docent Hanindyo Kuncarayakti
Prof. Seppo Mattila

The originality of this thesis has been checked in accordance with the University of Turku quality assurance system using Turnitin Originality Check service.

UNIVERSITY OF TURKU
Department of Physics and Astronomy

Koivisto, Niilo Observational study of the type IIb supernovae 2017gkk and 2019gaf

Master's thesis, 46 pp.
Astronomy
December 2022

Supernova (SN) is bright explosion of a star at the end point of stellar evolution. Supernova explosions caused by gravitational collapse of the core of the star are called core-collapse supernovae (CCSNe), which can be classified to several types, such as II, Ib and Ibc, based on their spectral features. Type II shows strong hydrogen (H) features, type IIb shows weak H features and Ibc shows no H features. Strength of the features reflects the amount H in the envelope of their progenitors at explosion, which depends on their mass loss history.

The progenitor stars of type Ibc SNe have lost their H envelope through mass loss, as for type II SNe H envelope of the SN progenitor are intact at explosion. Type IIb SNe are intermediate case of these types.

The mechanism for the mass loss is unclear. In general, massive stars have two major mass loss processes: the stellar wind and the binary effects. Stars with higher mass and higher metallicity have stronger stellar winds, which suggest that these properties of the progenitor star should determine the type the SN explosion. In case that the mass loss is caused mainly by the binary effects, the mass loss would be affected by the binary parameters rather than the properties of the progenitor. This connection between the mass loss mechanism and the observational properties of SNe enables us to investigate the origin of SN progenitors.

In this thesis, I used the photometric and spectroscopic observations on SNe 2017gkk and 2019gaf to study the properties of the progenitor stars and the SNe explosions. In particular, I derived the progenitor mass and explosion properties such as the ejecta mass, the ejecta velocity, the ^{56}Ni mass and the rise time for both SN.

As a future work, I will compare these values to other type IIb SNe as well as other CCSNe, taken from the literature. These comparisons I will use to discuss the mass loss mechanism of the stripped envelope SN (SE SN) and the origin of the type IIb.

Keywords: Supernovae, Core-collapse supernovae, Type IIb SNe, SN 2017gkk, SN 2019gaf

Contents

Preface

1 Introduction

Supernovae (SNe) are explosions of stars at the end point of their evolution. Research on these transient events started in 1934 by Baade & Zwicky, who recognized the presence of SNe [1]. There are historical records on SNe even before this time. For example, there were Galactic SNe in 1604 and 1572. The closest SNe that has been observed with modern telescopes is SN 1987A in the Large Magellanic Cloud located at 50 kpc away from the Earth [2].

The number of discovered SNe has increased to thousands by the recent large transient surveys such as the Zwicky Transient Facility (ZTF) [3] [4], the Asteroid Terrestrial-impact Last Alert System (ATLAS) [5] and the Panoramic Survey Telescope and Rapid Response System (Pan-STARRS) [6]. In the future a next-generation transient survey, the Legacy Survey of Space and Time (LSST), is expected to find several millions of SNe on the course of the next ten years, which will enable us to study very rare types of SNe. [7].

Research on supernovae is closely linked to other fields in astronomy, e.g. stellar evolution, star formation, chemical evolution and cosmology. For example, type Ia SNe have been used as a standard candle in cosmology. [8] [9]

1.1 Classification of supernovae

SNe are classified based on their spectral and photometric features (see Figure 1 and Figure 2). The main classes of SNe are type I, which do not have hydrogen lines in their spectra, and type II which have. The peak brightness of SNe is typically around -19 mag for type Ia SNe and between ~ -15 mag and ~ -19 mag for type II SNe [10]. SNe typically reach the peak brightness within ~ 20 days after explosion.

Type I SNe are divided into three subclasses: type Ia SNe (which show strong

silicon lines), type Ib SNe (which show helium lines) and type Ic SNe (which show neither strong lines of silicon nor helium).

Type II SNe are divided to five subclasses: type IIn SNe (which show narrow hydrogen lines), type IIb SNe (which show hydrogen features only in early phases), type IIP SNe (which show a plateu in their light curves) and type IIL SNe (whose light curves linearly decline). The plateau phases of type IIP SNe last typically for $\sim$ 100 days, followed by the sharper decline. This classification bases on the spectrum obtained at the peak brightness. [11] [12]

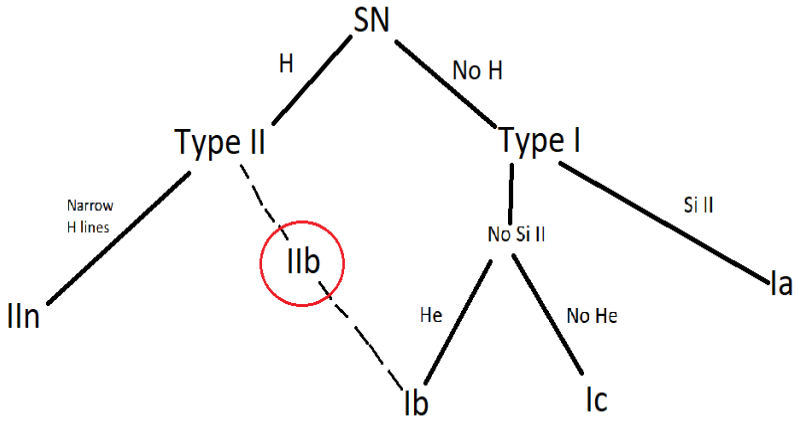

Figure 1. Classification of SNe based on which spectral lines are present in the spectrum. This thesis will focus on SN 2017gkk and SN 2019gaf which both are type IIb SNe.

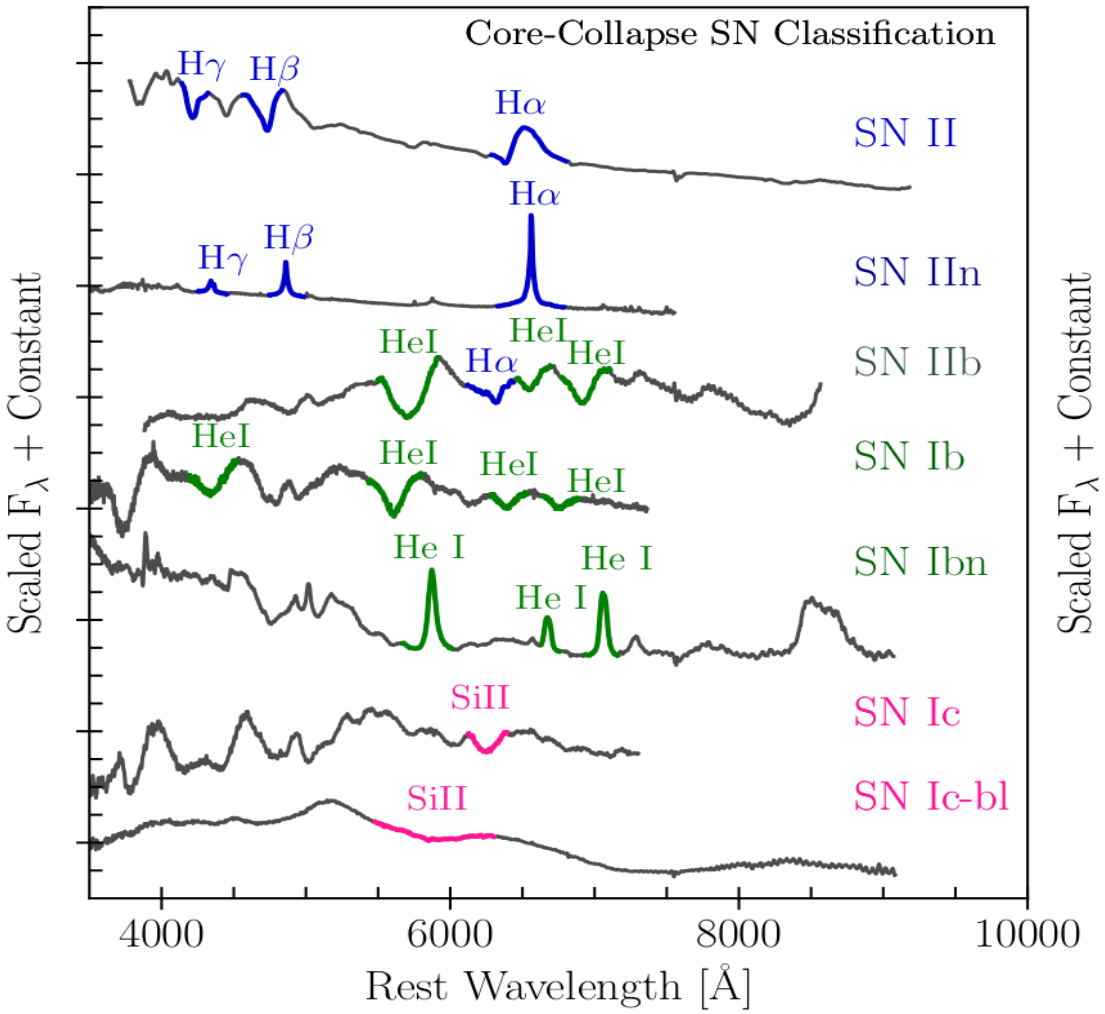

Figure 2. Typical spectra of core-collapse SNe, where defining lines are highlighted. Type IIb spectrum show hydrogen lines in early phase and prominent helium lines afterwards. [13]

In addition to the spectral and the photometric features, SNe can also be classified by their explosion mechanisms to thermonuclear SNe (type Ia) and core-collapse SNe (all types II, type Ic and type Ib). Thermonuclear SNe explode due to the energy released by thermonuclear runaway in a carbon-oxygen white dwarfs (WD), while core-collapse SNe (CCSNe) explodes due to the energy released by the collapse of stellar core in a massive star [14]. CCSNe are discussed in more detail in section 1.2. The progenitors of type Ia SNe are WDs in binary systems. In the classical scenario, the gas from the companion star is accreted by the WD. Once its

mass reaches the Chandrasekhar mass limit, it will start thermonuclear reactions in the central part, which causes SN explosion. [9]

1.2 Explosion mechanism

The explosion mechanism of CCSNe highly depends on their progenitor mass, but it is also affected by other factors such as their progenitors's metallicity and binarity.

At the beginning of their evolutions, stars consist of mostly hydrogen. Throughout their lives, they create heavier elements by nuclear fusion reactions. Iron is the final product of the stellar nucleosynthesis, because iron is the most stable element and thus its fusion reaction is endothermic. This leads to situation that at the end point of stellar evolution massive stars have iron core.

The iron core is supported by the degeneracy pressure of electrons. [15] If an iron core is massive enough, it becomes marginally stable in the final phase of the evolution. In this case, electron capture reactions or photodisintegration of Fe can make the core unstable, causing its collapse.

In the electron capture reactions, protons in atomic nuclei change to neutrons by capturing free electrons, which are responsible for the degeneracy pressure supporting the core.

In the photodisintegration of Fe, it decomposes to ^{4}He which further decomposes into protons and neutrons while absorbing energy. In either case, the core loses energy and pressure, which prompts the collapse. [16]

This collapse is halted when the central density reaches the nuclear density and the degeneracy pressure of neutrons starts to repulse the falling matter. This creates a shock, which will propagate outward in the stellar envelope. [17]

Most of the energy released by the explosion escapes from the SN ejecta through neutrino radiation ($\sim 10^{53}$ erg), but $\sim 1\%$ of the energy is injected into the shock, which will accelerate and heat the ejecta as it propagates outwards. The rise of the

temperature in the ejecta triggers explosive nucleosynthesis in the postshock region producing heavy elements such as ^{56}Ni.

1.3 Stripped-envelope supernovae

As explained in section 1.1 SNe are classified based on their spectral and photometric features. Those spectral features depend on which elements are present in outer layers of SNe. In section 1.2 it is explained that massive stars synthesize heavy elements through their evolution. At the end of their lives, they have an onion-skin structure with successive shells containing the ashes of the various burning stages as presented in Figure 3.

From those SN types which were defined in section 1.1 IIb, Ib and Ic are considered as Stripped Envelope SNe (SE SNe). SE SNe can lose the envelopes through several mass-loss mechanisms. The degree of the envelope stripping in SN progenitors determines the observational properties of the SNe and thus their SN types. [18]

CCSNe which have no envelope stripping and show hydrogen features in all phases in their evolution are classified as type II SNe. If the H-envelope has been stripped completely the SN will be type Ib, but if there is still a small fraction of hydrogen left it can show hydrogen features in the early phase after the SN explosion and is classified as type IIb. In a case that both hydrogen and helium envelopes are completely stripped, the star will explode as type Ic SN. [18][19]

There are several mechanisms which can cause mass loss, but it is still unclear how these affect to progenitors of different SNe types. Stellar winds are flows of material from stellar atmosphere driven by radiation. Momentum which is transferred from radiation to material in stellar atmosphere depends on opacity of material. Opacity can be much higher in absorption lines and therefore contribute to mass loss. This process is called line-driven wind and it is the main mechanism for mas-

sive stars. Strength of line-driven wind is strongly dependent on metallicity because more complex ions have more possible energy level transitions and therefore higher opacity. [20] Stellar wind can also be driven by magnetic fields.

Mass loss can also be caused by interaction with a companion star through mass transfer, if the radius of the progenitor is close to the Roche limit. In this limit outer layers are in gravitational equipotential with companion star which causes mass flow to companion. [21][22]

In this thesis I study two type IIb SNe to understand mass loss mechanisms of their progenitors. For these two SN I derive parameters like ejecta mass, ^{56}Ni mass, progenitor mass, explosion energy and expansion velocity which can be used to constrain possible scenarios for the mass loss. [23]

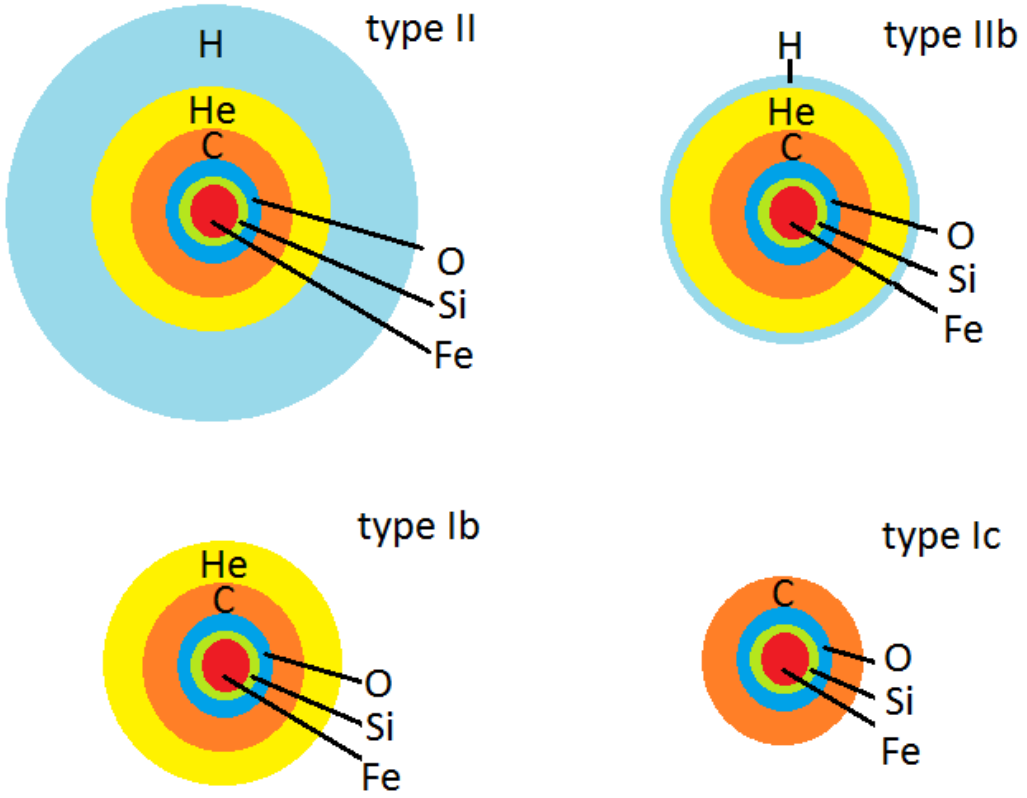

Figure 3. The stellar structure of the progenitors of core-collapse supernovae and which type of SN they produce.

1.4 SN 2017gkk

SN 2017gkk was discovered on 31.8.2017 by Koichi Itagaki [24] and classified on 2.9.2017 as a type IIb by NUTS (The NOT Unbiased Transient Survey)[25]. The redshift (z=0.004923) was obtained from the emission lines of the host galaxy NGC2748 [26]. The distance was assumed to be same as the host galaxy value 17.5 Mpc (corresponds to the distance modulus 31.2 mag), which was obtained using the Tully-Fisher relation [27]. The explosion date, 17.8.2017 (MJD 57982) was estimated from the pseudobolometric LC as explained in section 4.6. The values for the Milky Way extinction are taken from NASA/IPAC Extragalactic Database (NED [28])(A_B=0.097, A_V=0.073, A_R=0.058 and A_I=0.040). There was no Na I D absorption lines in spectra, which is why the extinction from the host galaxy was not considered.

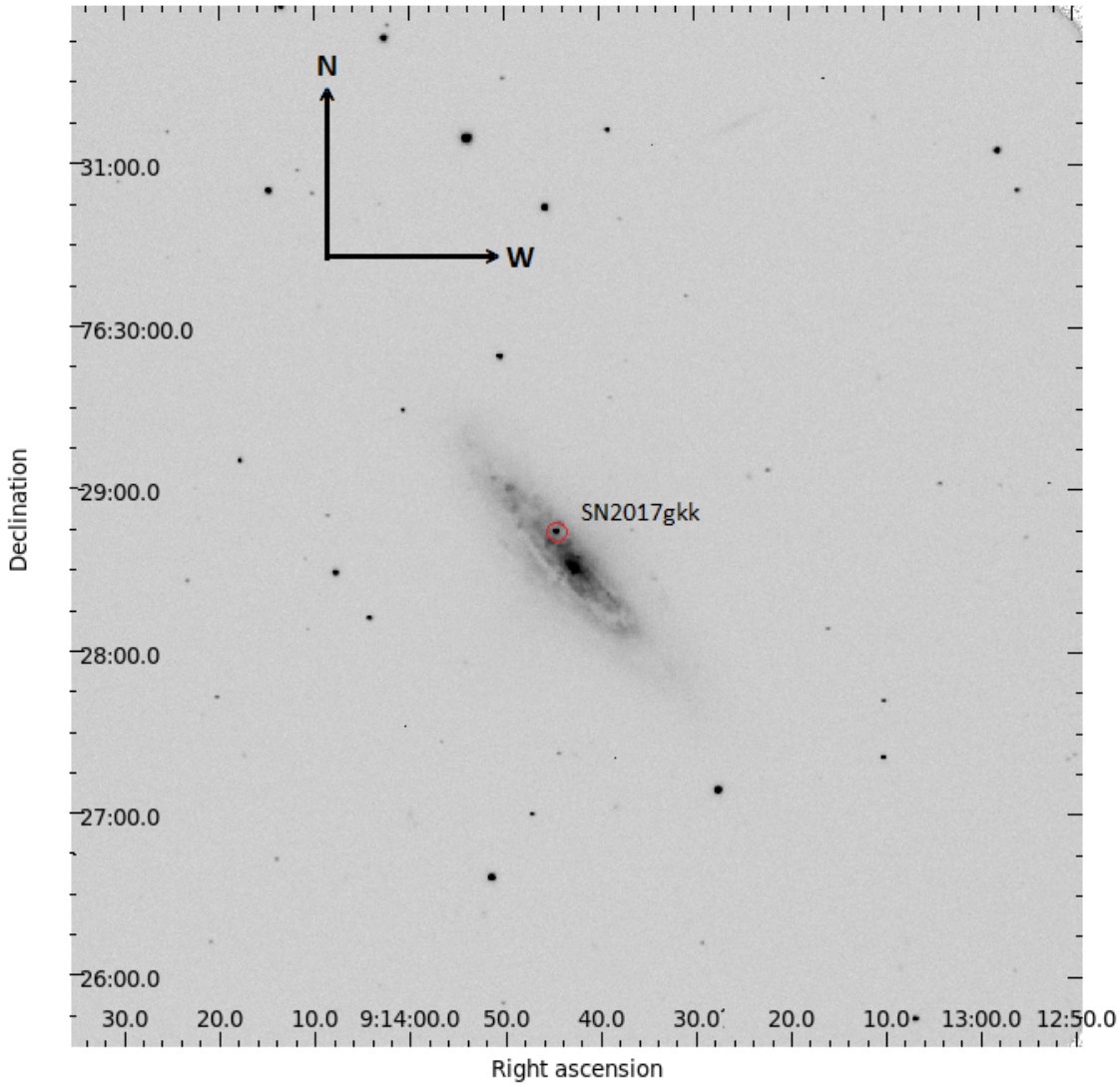

Figure 4. SN 2017gkk in NGC2748. R-band image obtained 18.9.2017 (32 days after explosion) with Nordic Optical Telescope using the ALFOSC instrument.

1.5 SN 2019gaf

SN 2019gaf was discovered on 27.5.2019 (MJD 8630.55) by the ATLAS survey [29] and classified on 1.6.2019 [30] as a type IIb by advanced Public ESO Spectroscopic Survey for Transient Objects (ePESSTO+) [30]. Its latest non-detection was 25.5.2019 (MJD 58628.56) by ATLAS which gives the limit for possible explosion date [5]. In this thesis, the explosion date 26.5.2019 (MJD 58629.6), is assumed

to be at the midpoint between the latest non-detection date and the discovery date. The redshift (z=0.0196) was derived from latest spectrum (203 days after explosion) using narrow [O III] 5007 Å and Hα lines (assumed to be from the host).

Distance to SN 2019gaf was calculated with Ned Wright's Javascript Cosmology Calculator [31] using the redshift, 73.4 km s^{-1} Mpc^{-1} [32] as Hubble constant, 0.286 [33] as Ω_m and 0.714 [33] as Ω_{vac}. The luminosity distance derived from this method was 81.3 Mpc, which corresponds to the distance modulus of 34.6 mag. The values for the Galactic extinction are taken from NASA/IPAC Extragalactic Database (NED [34])(A_g=0.343, A_r=0.237, A_i=0.176 and A_z=0.131). There was no Na I D absorption lines in spectra, which is why the extinction from the host galaxy was not considered.

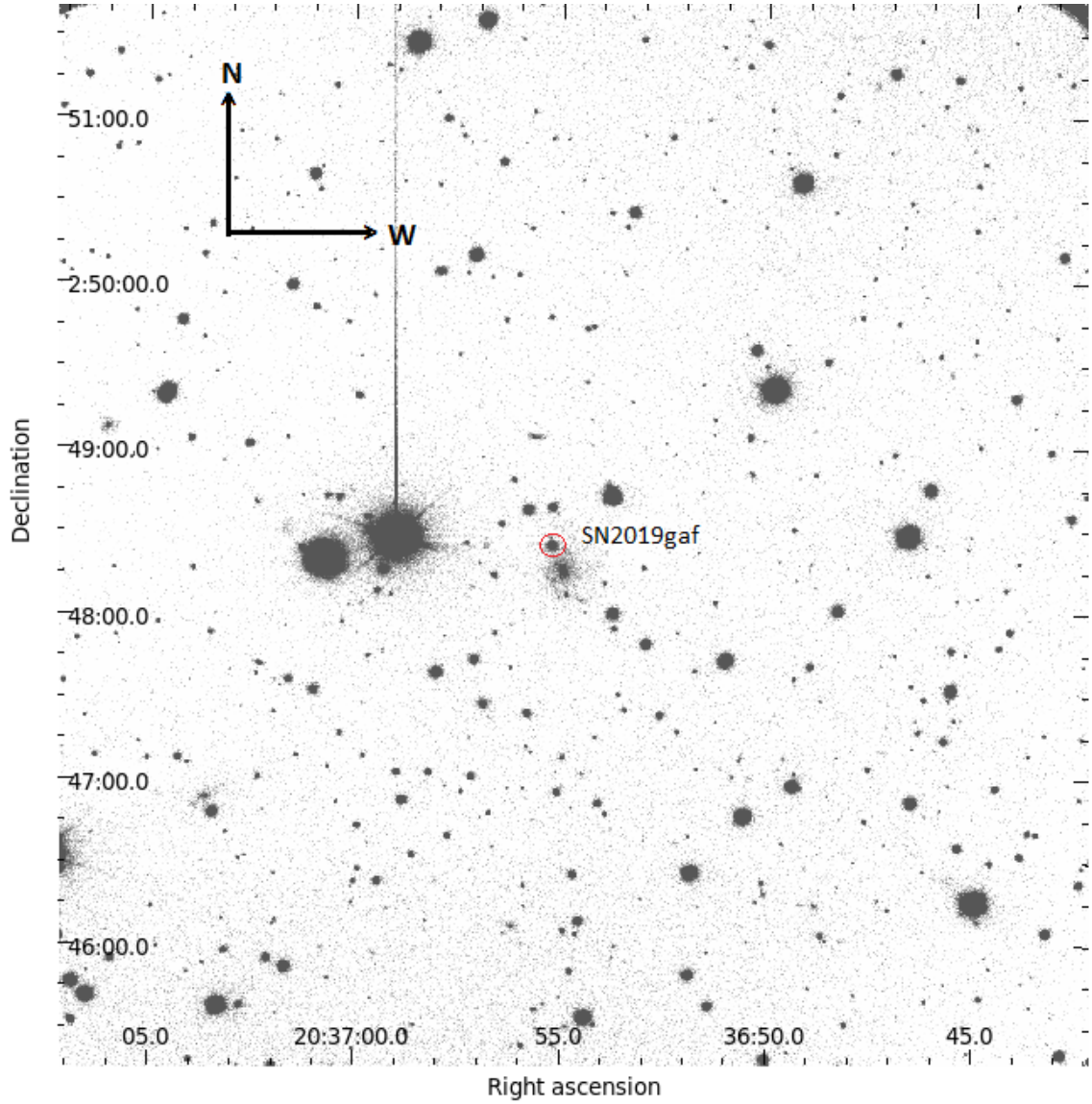

Figure 5. SN 2019gaf near LEDA 1237919 [35]. Image obtained 6.6.2019 (10 days after explosion) in r-band with Nordic Optical Telescope using the ALFOSC instrument.

2 Observations and Data reduction

2.1 Observations

Photometric (*BVRIgriz* bands) and spectroscopic data used in this thesis were obtained with Andalucia Faint Object Spectrograph and Camera (ALFOSC) on the

Nordic Optical Telescope (NOT) through NOT Unbiased Transient Survey (NUTS) collaboration. The photometric data for SN 2017gkk were obtained at 12 epochs from 15.9.2017 to 7.12.2018, while those for SN 2019gaf were acquired at 10 epochs from 3.6.2019 to 22.11.2019. The spectroscopic data for SN 2017gkk were obtained at 9 epochs from 2.9.2017 to 15.2.2018, while those for SN 2019gaf were acquired at 9 epochs from 3.6.2019 to 14.12.2019.

2.2 Data reduction for photometry

All the images were reduced with bias subtraction and flat-field correction, using the Image Reduction and Analysis Facility (IRAF) [36]. The bias subtraction was done using a masterbias image which was the average of 11 bias images, taken in same nights as the observations. The flat-field correction was done using average of three sky flat-field images for each band, and applied it to the corresponding science images.

2.3 Data reduction for spectroscopy

The spectroscopic data were reduced and analyzed using ALFOSCGUI [37]. It is a graphic interface pipeline designed to reduce observational data from the ALFOSC instrument on the NOT. It can be used for both spectroscopic and photometric reductions, but in this thesis it has been used only for spectroscopy. ALFOSCGUI recognizes keywords such as imagetype from the FITS headers and performs all basic reduction processes such as bias reduction, flat-field correction, spectral extraction, wavelength correction, flux calibrations and removal of telluric absorption lines using IRAF tasks in pyraf. Master bias was the average from 11 bias images. Master flat field was averaged from 5 halogen-lamp images taken in the same night as observations using the same grism and slit as in the science images. For wavelength calibration ALFOSCGUI used calibration frames taken with HeNe lamps during

the same night using the same grism and slit as in the science images. The flux calibration was done using a standard star observed with the same setup with the science spectra in the same night.

2.3.1 Comparison of using IRAF and ALFOSCGUI

For one spectrum reduction and analysis were done completely with IRAF under Pyraf. The purpose for this was to compare results with ALFOSCGUI-reduced spectrum. In figure 6 we can see the spectrum, which was manually reduced with IRAF, is less noisy, but the spectrum, which was reduced with ALFOSCGUI, is good enough for analysis. The difference between the IRAF and the ALFOSCGUI spectra comes from the adopted values for the parameters during extraction process and there is no significant systematic differences between the two.

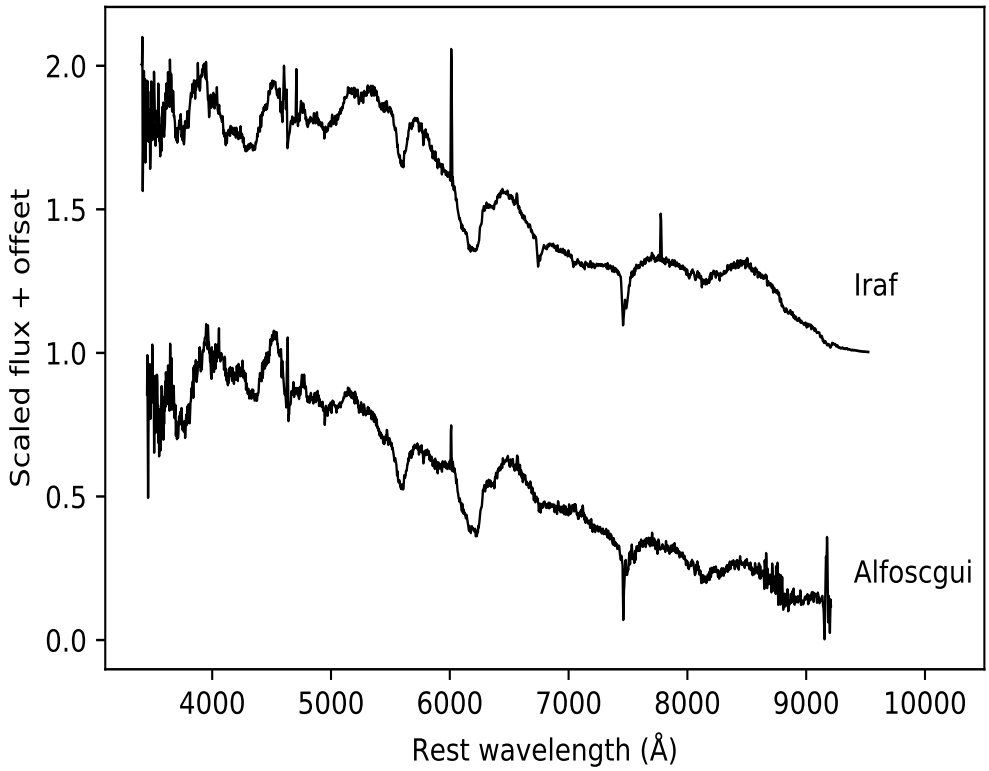

Figure 6. Comparison of SN 2019gaf spectrum from 3.6.2019 reduced with IRAF and same spectrum reduced with ALFOSCGUI.

3 Methods

3.1 Photometric measurements

The photometry of the SNe was conducted using AUTOmated Photometry Of Transients (AutoPhot) [38] based on Point Spread Function (PSF) fitting. The PSF describes the flux distribution that results from a point source in the image plane. AutoPhot uses a differential photometry, meaning that it measures instrumental magnitudes for the science target and the reference stars, which have known true magnitudes from the literature. The average difference between the instrumental magnitude and the apparent magnitude, i.e. zeropoint magnitude is reduced from

the instrumental magnitude of the science target, which gives us apparent magnitude of the science target. [39] The brightness of reference stars were adopted from the Panoramic Survey Telescope and Rapid Response System (Pan-Starrs) catalog [6] (griz bands) or the AAVSO Photometric All-Sky Survey (APASS) catalog [40] (BVRI). Since there is no available reference star in the u-band images, I did not use them in this study. The quality of the PSF fitting is different in different images. Some results were not usable. Figures 8 - 11 show examples of the failed fittings and a successful fitting. The details on the quality of the PSF fittings are shown in table II for SN 2017gkk and table IV for SN 2019gaf.

3.1.1 AutoPhot PSF model

In this thesis AutoPhot is used to build PSF models and measure the brightness of objects. First step is to determine the Full Width at Half Maximum (FWHM) of point sources in the image. AutoPhot finds point sources from the image and fits 2D Moffat function to these sources. FWHM values are assumed to follow a normal distribution so those sources which FWHM value is over 3 sigma away from the median value of FWHM, are clipped away. Next AutoPhot fits the 2D Moffat function to point sources in the image, subtracts it and measures the average residual image, which represents the average background level. This PSF model can then be used to determine the counts for any source in the image. In this work template subtraction is not used.

The formula for the PSF model is

$$PSF(x, y, A) = M(x_0, y_0, A, FWHM) + R(x_0, y_0, A) \quad (1)$$

where M is the 2D Moffat function, A is the amplitude of the PSF, R is the residual, x and y are the pixel coordinates in image. x_0 and y_0 are the pixel coordinates respect to the center of the source.

3.1.2 Target magnitude error

The errors for the magnitudes of the targets are calculated as follows:

$$\delta m = \sqrt{\delta m_{inst}^2 + \delta ZP^2} \tag{2}$$

Here, δm_{inst} is the photon shot noise for the targets, calculated as follows from the signal to noise ratio:

$$\delta m_{inst} = 2.5 log_{10}(1 + \frac{1}{S/N}) \approx 1.0875(\frac{1}{S/N}) \tag{3}$$

δZP is the standard deviation of zeropoint magnitudes of all reference stars. [38]

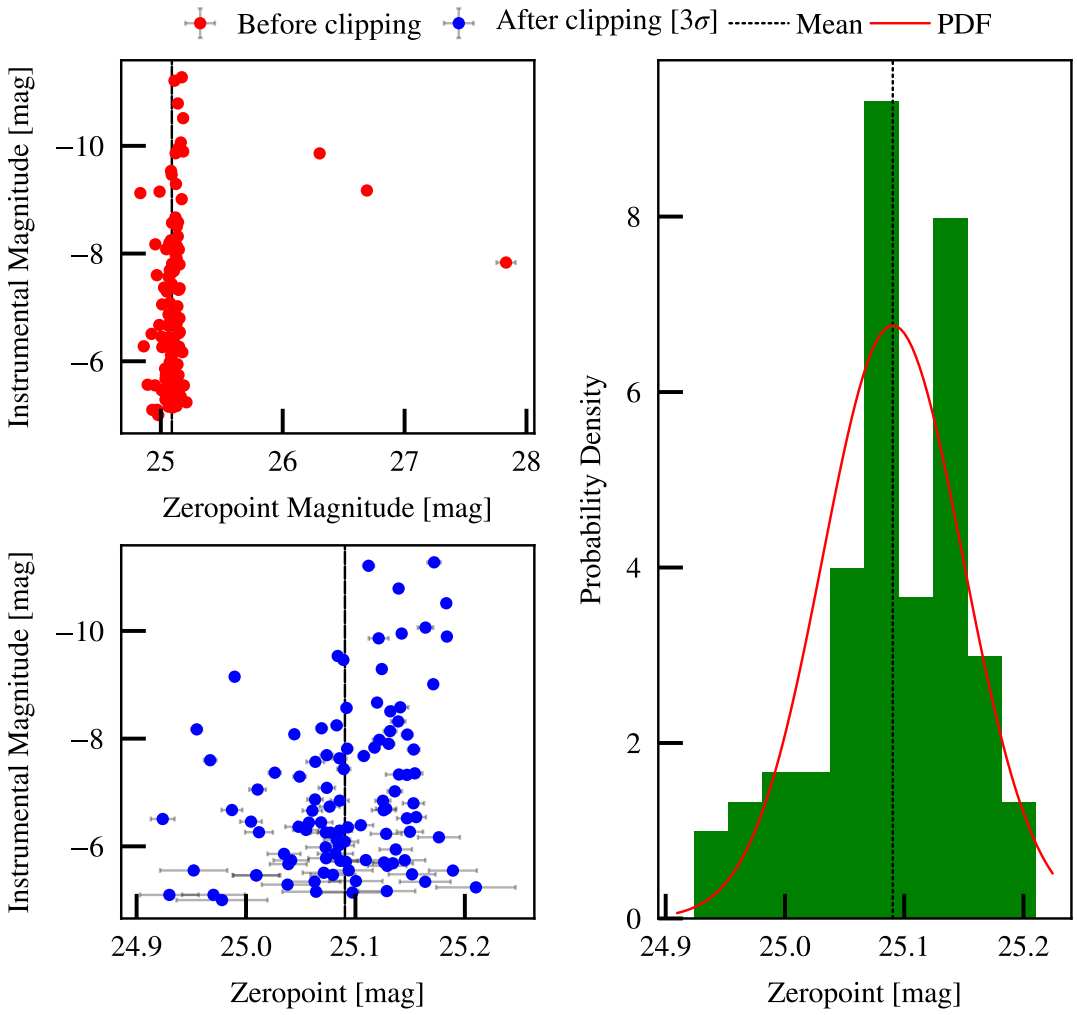

Figure 7. Example of zeropoint measurement using image from SN 2019gaf in r-band at MJD 58638. The panel at upper left corner presents distribution of the instrumental magnitudes versus the zeropoint magnitudes of all reference stars, which AutoPhot found from the image. The panel at the lower left corner is the same distribution after reference stars which zeropoint magnitudes differ over 3 σ were clipped away. The panel at the right shows probability density function (PDF) of the zeropoint magnitudes and the normal distribution fitted to those values.

3.1.3 Target detection probability

The target detection probability is the probability to judge if the detected sources as a target are real or just noise. This is based on the signal to noise ratio. AutoPhot also uses the offset of the flux peak of a target to judge if the sources are real. In

this thesis, if the offset is more than 10 pixels, the detected target is considered fake. Comparing Tables II and IV and Figures 8-11, we can see that the detections with higher offsets than 10 pixels or with target detection probabilities less than 0.1 can be regarded as unreliable detections.

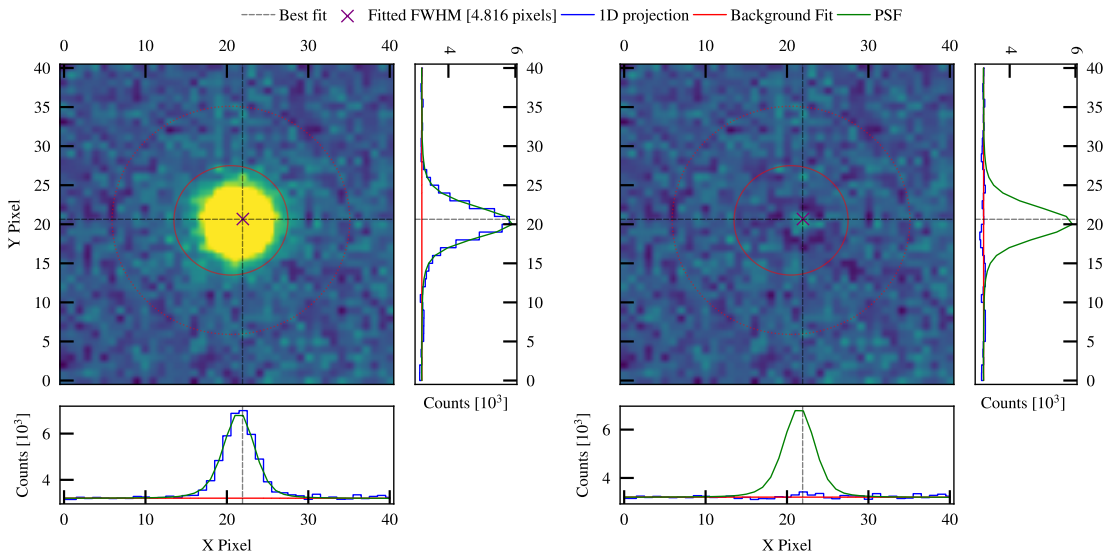

Figure 8. Example of succesful PSF fitting. In this figure AutoPhot has used r-band image of SN 2019gaf obtained at 12.6.2019 (MJD 58646, 16 days after explosion). The image on the left show the target before the subtraction. The image on the right shows the residual image after the subtraction of the PSF fit. The small panels on the bottom and on the right of the images show the count distribution in respect to X- or Y-axis.

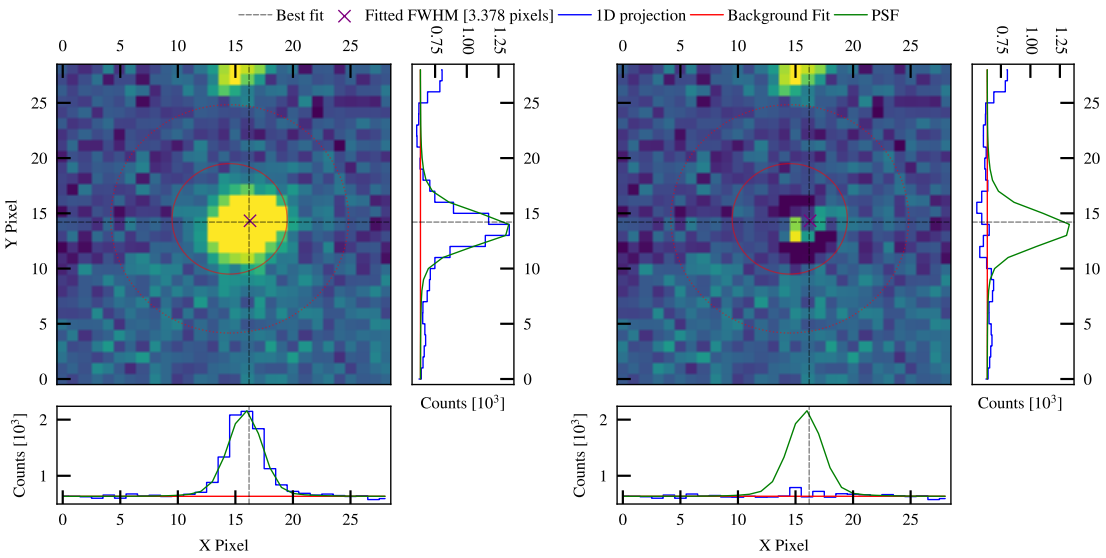

Figure 9. Example of PSF fitting where we can see small errors, but result is still usable. In this figure AutoPhot has used r-band image of SN 2019gaf obtained 17.9.2019 (MJD 58744, 114 days after explosion).

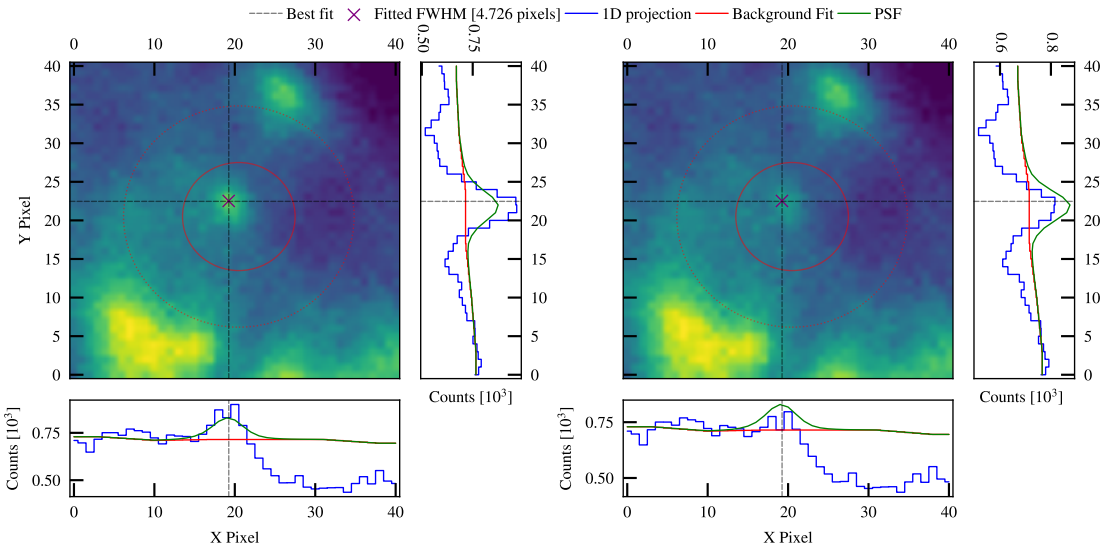

Figure 10. Example of PSF fitting where it is difficult to see if results are reliable, so we should be cautious with the results. In this figure AutoPhot has used V-band image of SN 2017gkk obtained 14.2.2018 (MJD 58163, 181 days after explosion).

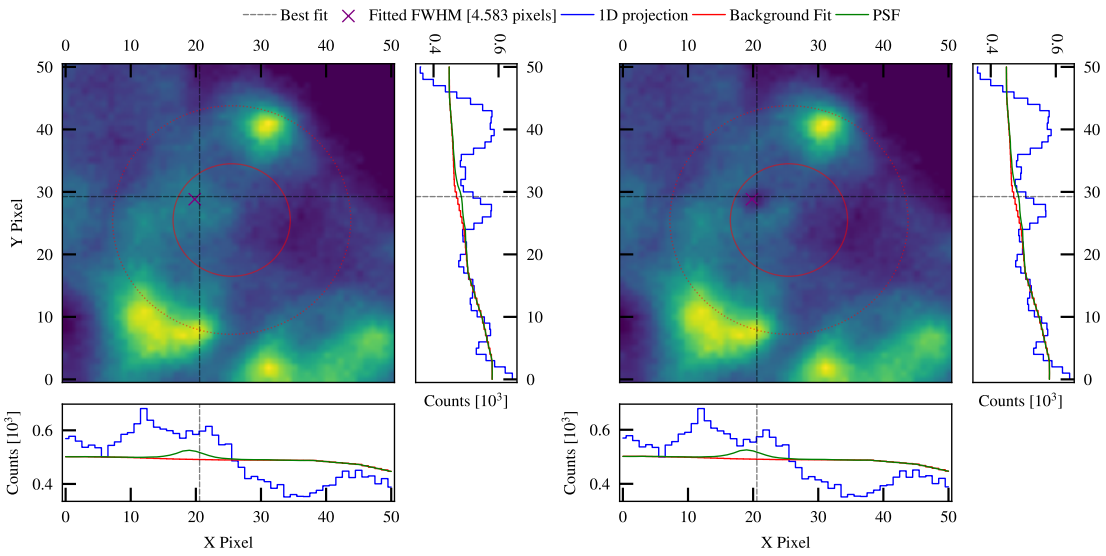

Figure 11. Example of PSF fitting where AutoPhot has failed to produce accurate PSF fit, so result are unusable. In this figure AutoPhot has used B-band image of SN 2017gkk obtained 10.5.2018 (MJD 58248, 266 days after explosion).

MJD	B	err	V	err	R	err	I	err
58015	18.46	0.15	16.88	0.05	16.24	0.08	15.94	0.14
58024	18.93	0.12	17.38	0.08	16.67	0.08	16.39	0.12
58027	18.99	0.12	17.46	0.07	16.81	0.06	16.47	0.09
58036	19.15	0.14	17.71	0.13	17.08	0.13	16.66	0.17
58075	-	-	18.31	0.28	18.00	0.24	17.48	0.16
58094	19.70	0.12	18.74	0.11	18.48	0.06	17.91	0.09
58116	19.69	0.21	18.85	0.25	18.60	0.08	18.17	0.11
58163	-	-	20.90	0.31	19.42	0.10	-	-
58165	20.38	0.17	-	-	-	-	19.12	0.10
58219	-	-	20.21	0.20	19.96	0.19	-	-
58248	21.06	0.24	21.22	0.23	22.37	0.80	20.89	0.23
58460	18.49	0.09	17.88	0.10	17.67	0.07	19.03	0.20
58460	0.03	13.06	0.65	18.43	0.75	17.70	0.69	17.35

Table I. Photometric results of SN2017gkk from BVRI bands and errors.

	B		V		R		I	
MJD	dp	offset	dp	offset	dp	offset	dp	offset
58015	1.00	4.39	1.00	3.77	1.00	3.58	1.00	0.96
58024	1.00	5.29	1.00	4.91	1.00	1.85	1.00	3.58
58027	0.95	5.64	1.00	4.26	1.00	1.24	1.00	3.42
58036	0.99	3.48	1.00	2.81	1.00	2.29	1.00	2.91
58075	-	-	0.06	4.64	0.10	5.26	0.58	1.05
58094	0.49	4.86	0.98	3.68	1.00	3.55	1.00	2.09
58116	0.15	8.42	0.19	6.81	0.47	2.94	0.31	4.82
58163	-	-	0.02	2.33	0.91	1.22	-	-
58165	0.11	4.49	-	-	-	-	0.53	2.61
58219	-	-	0.03	7.50	0.04	3.97	-	-
58248	0.07	6.19	0.04	3.88	0.00	1.82	0.03	2.46
58460	0.65	18.43	0.69	17.35	0.75	17.70	0.03	13.06

Table II. Quality of photometric reductions of SN 2017gkk from BVRI -bands. In this table dp is the detection probability (number between 0 and 1) and offset the difference (in pixels) between the best fit location and assumed location of the target based on coordinates from FITS-image.

MJD	g	err	r	err	i	err	z	err
58638	17.49	0.07	17.41	0.08	17.51	0.10	17.60	0.10
58641	17.48	0.04	17.25	0.04	17.29	0.09	17.37	0.08
58646	17.70	0.05	17.23	0.05	17.20	0.05	17.21	0.07
58647	17.74	0.05	17.23	0.06	17.20	0.09	17.25	0.09
58652	18.11	0.07	17.38	0.07	17.27	0.10	17.25	0.12
58654	18.31	0.05	17.50	0.09	17.36	0.07	17.32	0.07
58709	20.06	0.13	19.24	0.08	19.01	0.11	19.27	0.06
58744	20.53	0.08	19.71	0.13	19.59	0.17	19.61	0.15
58766	20.75	0.17	19.85	0.10	19.93	0.14	20.60	0.24
58810	21.26	0.08	20.41	0.08	20.68	0.12	-	-

Table III. Photometric results of SN 2019gaf from griz -bands and errors.

	g		r		i		z	
MJD	dp	offset	dp	offset	dp	offset	dp	offset
58638	1.00	1.72	1.00	1.85	1.00	1.31	1.00	2.94
58641	1.00	1.06	1.00	1.24	1.00	1.82	1.00	1.34
58646	1.00	1.24	1.00	1.43	1.00	1.31	1.00	1.76
58647	1.00	1.39	1.00	1.22	1.00	1.50	1.00	1.15
58652	1.00	1.70	1.00	1.96	1.00	1.47	1.00	1.62
58654	1.00	1.46	1.00	1.76	1.00	0.99	1.00	1.33
58709	1.00	1.13	1.00	1.59	1.00	1.29	1.00	0.00
58744	1.00	1.66	1.00	1.71	1.00	2.14	1.00	1.40
58766	0.90	1.25	1.00	1.34	1.00	1.32	0.98	1.68
58810	1.00	1.45	1.00	1.46	1.00	1.50	-	-

Table IV. Quality of photometric reductions from SN 2019gaf from griz -bands. See explanation for columns from table II.

3.2 Derivation of bolometric light curves

The pseudobolometric light curves of SNe 2017gkk and 2019gaf were constructed using the following method. The intrinsic absolute flux for a target was derived using equation 4.

$$f_X = f_{0X} 10^{-0.4 \cdot (m_X - dm_{SN} - e_{X,SN})} \tag{4}$$

where f_X is flux for the X band, m_X is the observed magnitude of the target in the X band, dm_{SN} is the distance modulus of the target, $e_{X,SN}$ is the Galactic

extinction for the target and f_{0X} is the zero-point flux flux for the X band.

Pseudobolometric magnitude was derived using equation 5

$$M = -2.5 \cdot log_{10}(\frac{f_X + f_Y + ...}{f_{0X} + f_{0Y} + ...}) \tag{5}$$

where f_X is flux for the X band, f_Y is flux for the Y band, f_{0X} is the zeropoint flux for the X band and f_{0Y} is the zeropoint flux for the Y band. The zeropoint fluxes from different bands are combined, which gives the zeropoint flux for combined flux from all available bands.

To obtain apparent magnitudes for all the bands at each every epoch I interpolated/extrapolated linearly from the nearest data points. This treatment might have produced inaccurate magnitudes of comparison object SN 1993J at early phases.

The pseudobolometric light curve for SN 2019gaf was constructed using the g-, r-, i- and z-band data, while the for SN 2017gkk was done using the B-, V-, R- and I-bands data.

For comparison, the pseudobolometric light curves were constructed for SNe 1993J and 2008ax using the U-, B-, V-, R- and I-bands data obtained from The Open Astronomy Catalog API (OACAPI)[41]. The data for SN 1993J were originally from [42] [43] [44] [45] [46] [47] [48] [49] [50] and for SN 2008ax from [51] [52] [53].

The zero-point fluxes were from [54].

For SNe 2017gkk and 2019gaf, the extinction from their host galaxies was assumed to be negligible. Only the Galactic extinction was considered in this work [28].

For SN 1993J and SN 2008ax total extinctions in V-band were adopted from [55] and [53], where extinctions were derived using various techniques such as strength of Na I D absorption. Total extinction in other bands were estimated using relation from [56]. Distance of SN 1993J was adopted from [42] and distance of SN 2008ax from [53].

3.3 Velocity measurements

The line velocities of Hα, He I and Fe II were estimated from the position of their absorption minima using IRAF splot task in onedspec package.

Figures 24, 23 and 24 show the time evolution of the derived line velocities, compared to the reference SNe 1993J and 2008ax.

4 Results

4.1 Spectral evolution

Figure 12 shows that for SN 2017gkk Hα P-cygni line is visible at least 54 days after explosion and disappears between 54 and 93 days. Spectra of SN 2017gkk shows He I 5876 Å line in spectra obtained between 30 and 93 days after explosion. 134 days after explosion [Ca II] 7291, 7323 Å and [O I] 6300, 6364 Å are visible. Ca II triplet at near-infrared is visible in all spectra from 17 days to 183 day.

Figure 13 shows that for SN 2019gaf Hα P-cygni line is visible at least 45 days after explosion and disappears between 45 and 82 days. Spectra of SN 2019gaf shows prominent He I 5876 Å line, except for latest spectrum obtained 202 days after explosion, where [Ca II] 7291, 7323 Å and [O I] 6300, 6364 Å are the most strongest lines.

Figure 14 shows a comparison of SNe 1993J and 2017gkk spectral evolution. Ca II triplet at near-infrared is visible from 22 days to 136 days. Line at 7601 Å is a telluric feature.

Figure 15 shows a comparison of SNe 1993J and 2019gaf spectral evolution. Line at 7601 Å is a telluric feature.

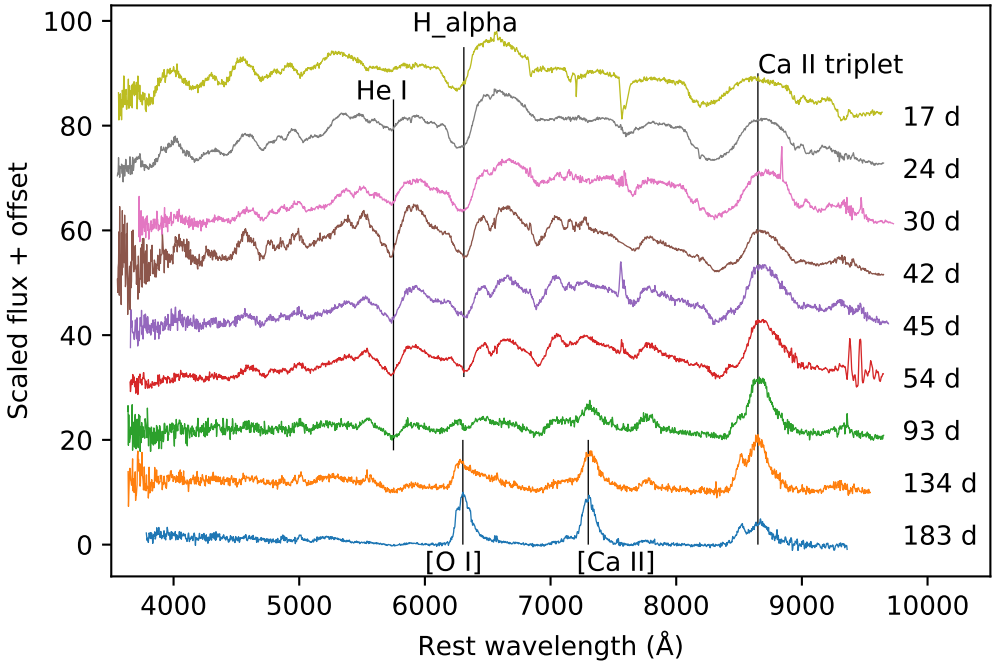

Figure 12. Time series of SN 2017gkk spectra. Days from explosion (MJD 57982).

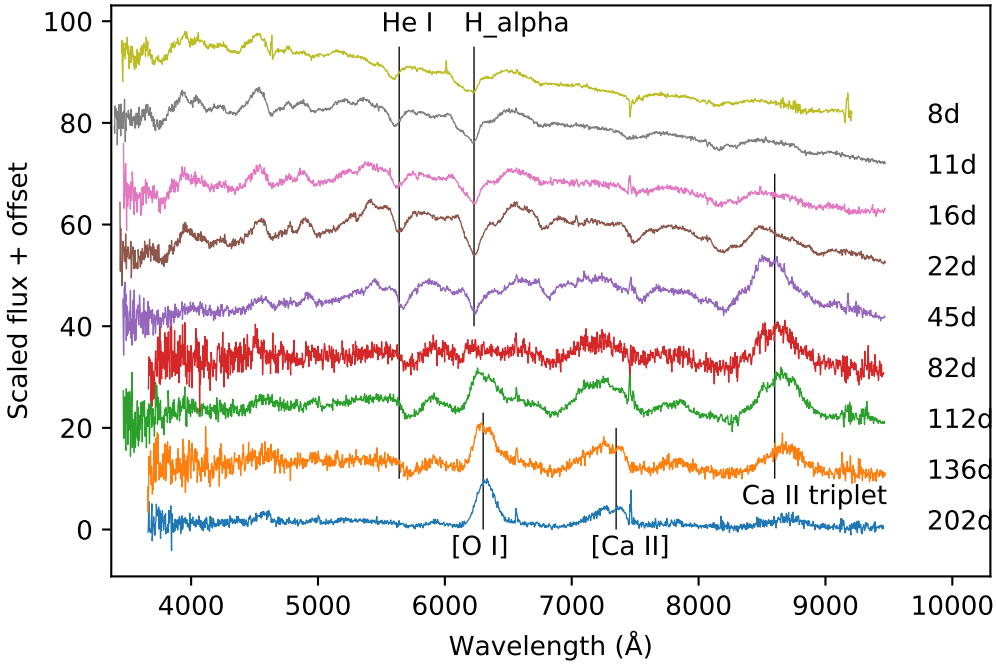

Figure 13. Time series of SN 2019gaf spectra. Days from explosion day (MJD 58629.6).

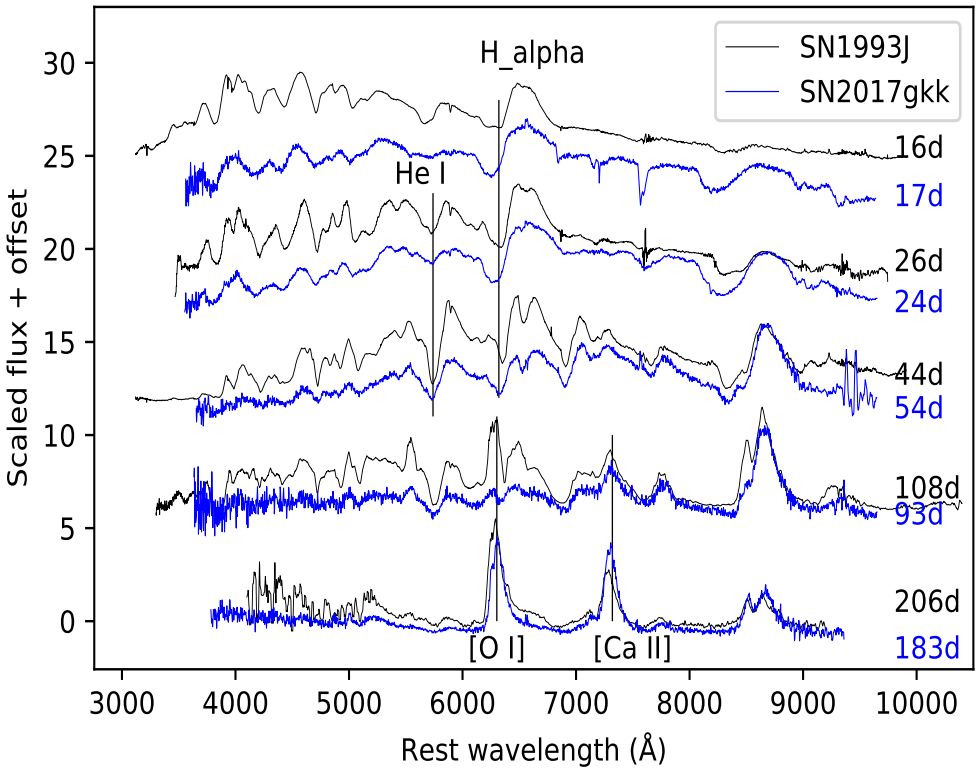

Figure 14. Spectral evolution comparison of SNe 2017gkk and 1993J. Days of spectra are respect to explosion date for both SN. Strongest telluric lines at 7603 Å has been removed from SN 2017gkk spectra.

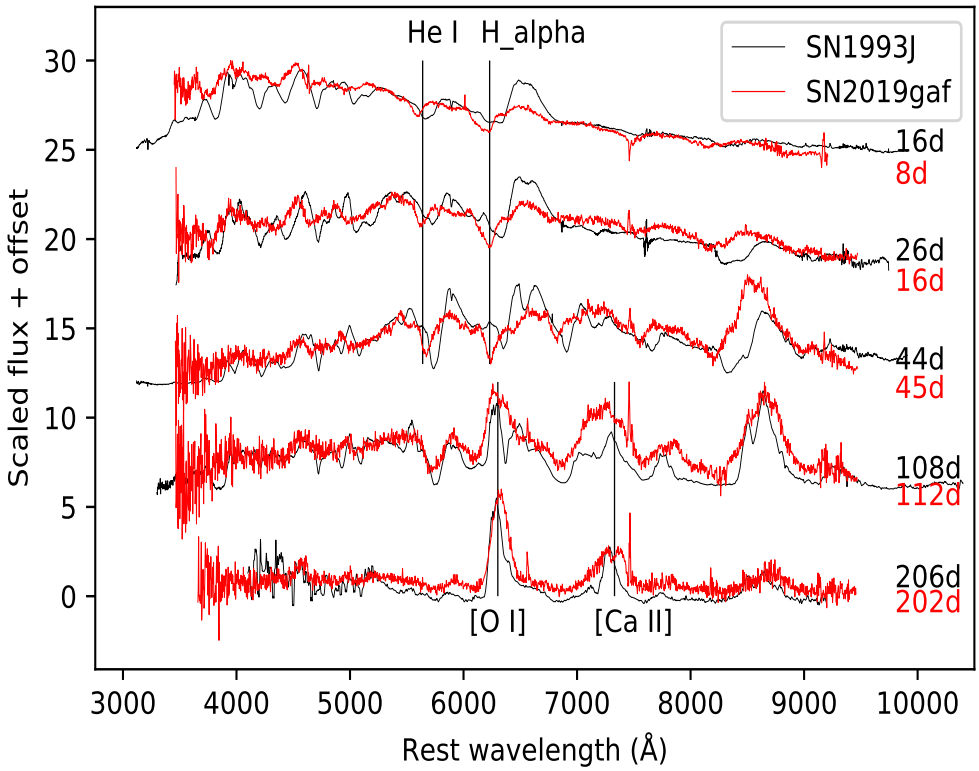

Figure 15. Spectral evolution comparison of SNe 2019gaf and 1993j. Days of spectra are respect to explosion date for both SN.

4.2 Light curves

Absolute magnitudes of SNe 2017gkk and 2019gaf were calculated using the following formula

$$M_{abs} = m_{app} - 5 \cdot log_{10}(d) + 5 - A \tag{6}$$

where m_{app} is apparent magnitude, d is distance of an SN in parsec and A is the Galactic extinction. Used distances and extinction are explained in sections 1.4 and 1.5.

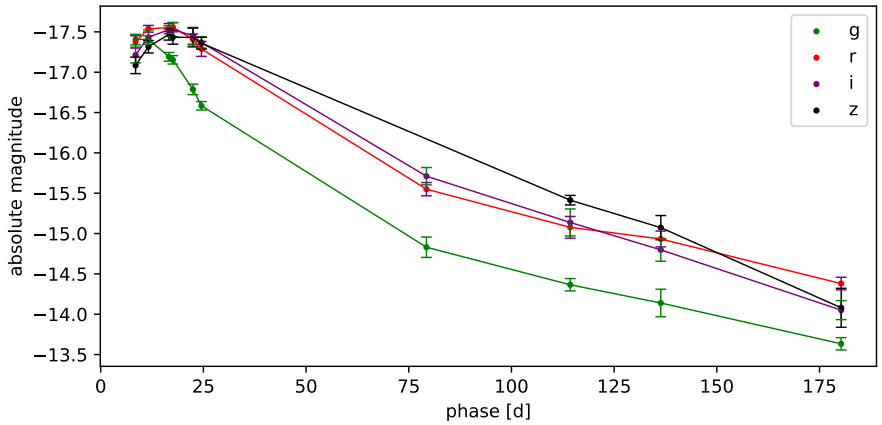

Figure 16. Absolute magnitude light curves of SN 2019gaf in g, r, i and z filters. Phase is from explosion (MJD 58629.6).

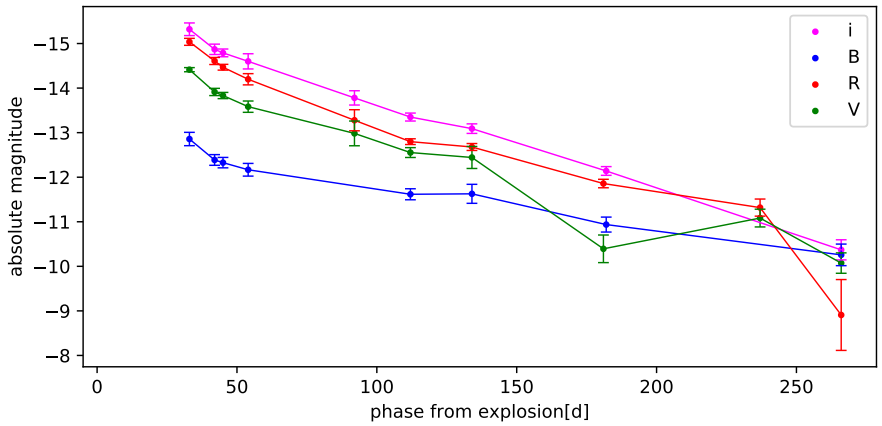

Figure 17. Absolute magnitude light curves of SN 2017gkk in B, V, R and i bands. Phase is from explosion (MJD 57982). As mentioned in section 3.1.3 PSF fitting was not reliable for all images, which probably explains drop in V band at 181 day. Latest observations at MJD 58460 are not presented for the same reason.

4.3 Color evolution

The color curves present how the difference of the brightness in two different bands evolves. In this thesis I present commonly-used color indexes g-i and r-i for SN 2019gaf and B-V and V-R for SN 2017gkk. Used extinction are explained in sections 1.4 and 1.5.

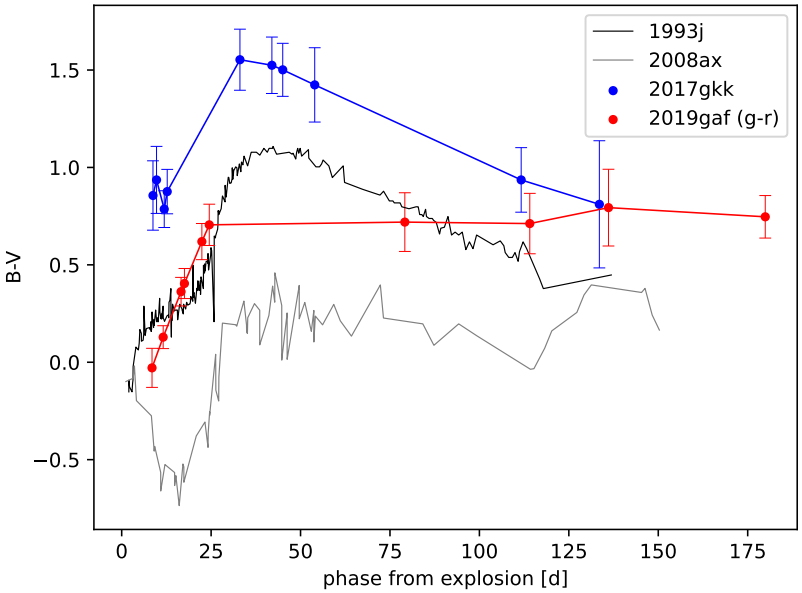

Figure 18. B-V color curve for SNe 1993J, 2008ax and 2017gkk and g-r color curve for SN 2019gaf. First 4 datapoints of SN 2017gkk from ATel [57].

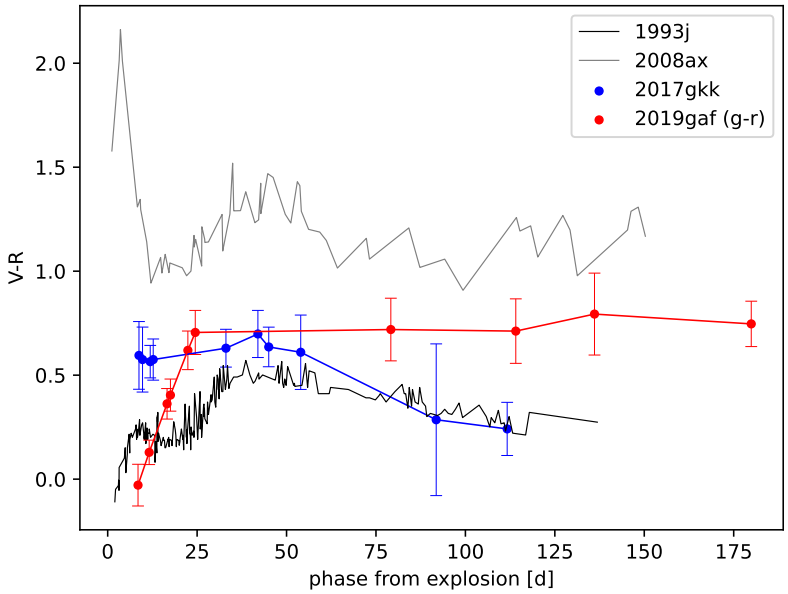

Figure 19. V-R color curve for SNe 1993J, 2008ax and 2017gkk and g-r color curve for SN 2019gaf. First 4 datapoints of SN 2017gkk from ATel [57].

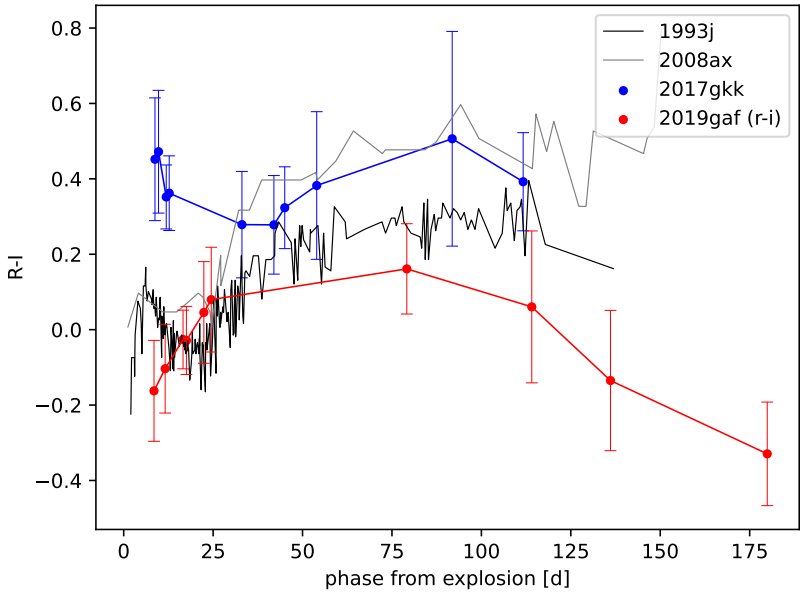

Figure 20. R-I color curve for SNe 1993J, 2008ax and 2017gkk and r-i color curve for SN 2019gaf. First 4 datapoints of SN 2017gkk from ATel [57].

4.4 Bolometric light curves

Bolometric light curves were constructed as explained in section 3.2. Figure 21 shows that SNe 2017gkk and 2019gaf did not show double peak feature as in SN 1993J. SN 2019gaf had similar peak brightness as SNe 1993J and 2008ax, but its rise time was around 3 days shorter. In tail phase, when light curve is powered radioactive decay of ^{56}Co, SN 2019gaf was bright compared to SNe 1993J and 2008ax. SN 2017gkk was much dimmer, but shape of the light curve was very similar to SN 1993J and SN 2008ax.

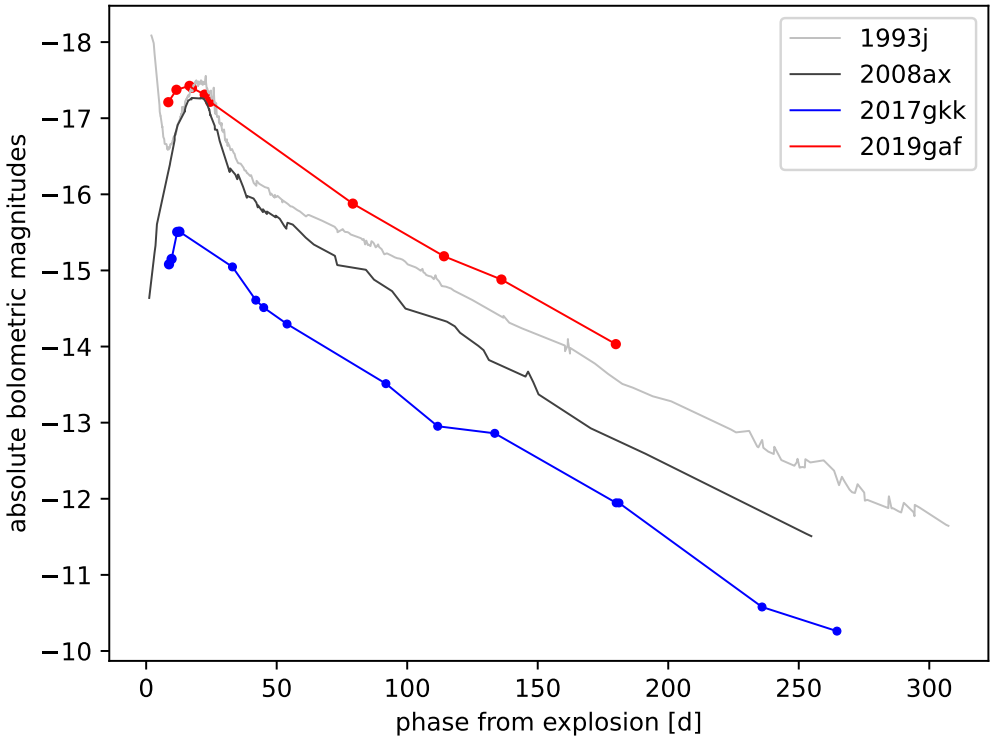

Figure 21. Comparison of bolometric light curves of SNe 1993J, 2008ax, 2017gkk anf 2019gaf. First 4 datapoints of SN 2017gkk from ATel [57].

4.5 Line velocities

Figure 24 shows that line velocity of Hα was quite stable for both SNe 2017gkk and 2019gaf as well for comparison SNe 1993J and 2008ax after 10 days from explosion. For SN 2017gkk velocity was between SNe 1993J and 2008ax, at around 12000 km/s. For SN 2019gaf velocity was higher at 16000 km/s.

Figure 23 shows that for SN 2017gkk He I 5876 line velocity is quite stable at around 8000 km/s, between comparison SNe 1993J and 2008ax. SN 2019gaf has around 2000 km/s higher He I line velocity, but it linearly declines from 14000 km/s to 8000 km/s between 10 and 80 days after explosion.

Figure 24 shows that line velocity of Fe II might be similar for all three SNe 1993J,

2017gkk and 2019gaf. Between 20 and 50 days after explosion velocity decreases from around 9000 km/s to 4500 km/s. SN 2019gaf has few datapoints which are probably unrealiable, first at 8 days after explosion is lower at 7000 km/s and later last two datapoints at 45 and 112 days at 8000 km/s. SN 1993J first datapoints is not at 9000 km/s, like SNe 2017gkk and 2019gaf, but in 7400 km/s, although it is otherwise similar.

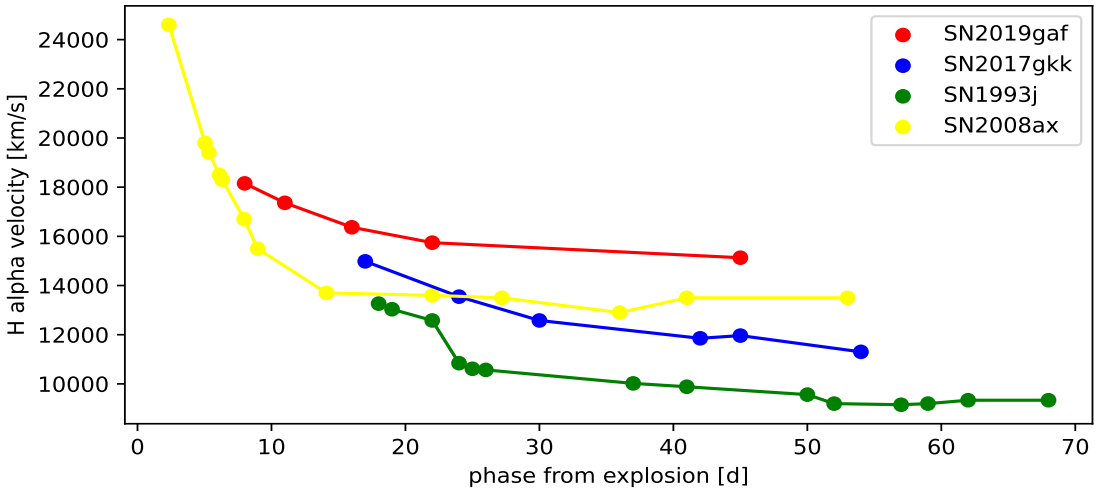

Figure 22. Comparison of velocity evolution of Hα. Data for SN 1993J were from [42] and for SN 2008ax from [58].

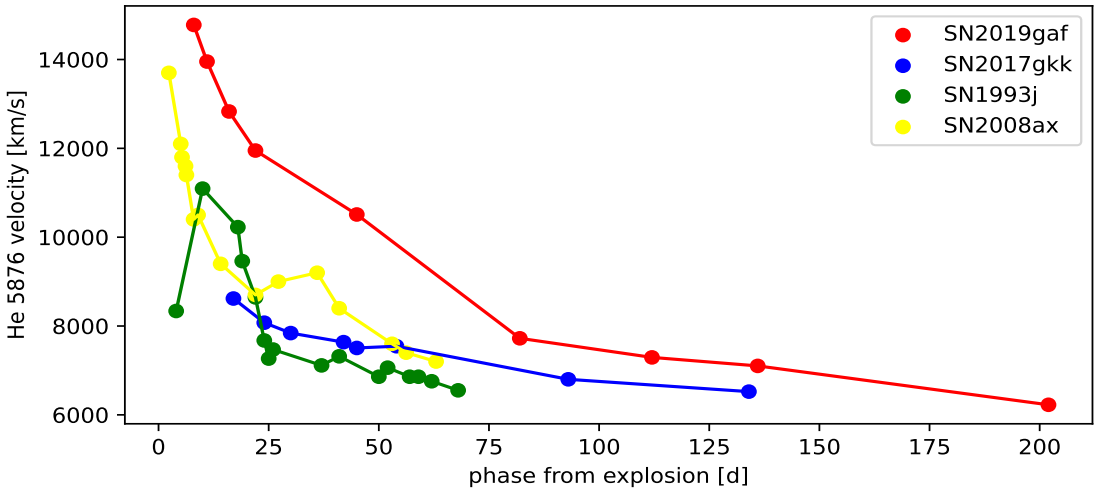

Figure 23. Comparison of velocity evolution of He I 5876. Data for SN 1993J were from [42] and for SN 2008ax from [58].

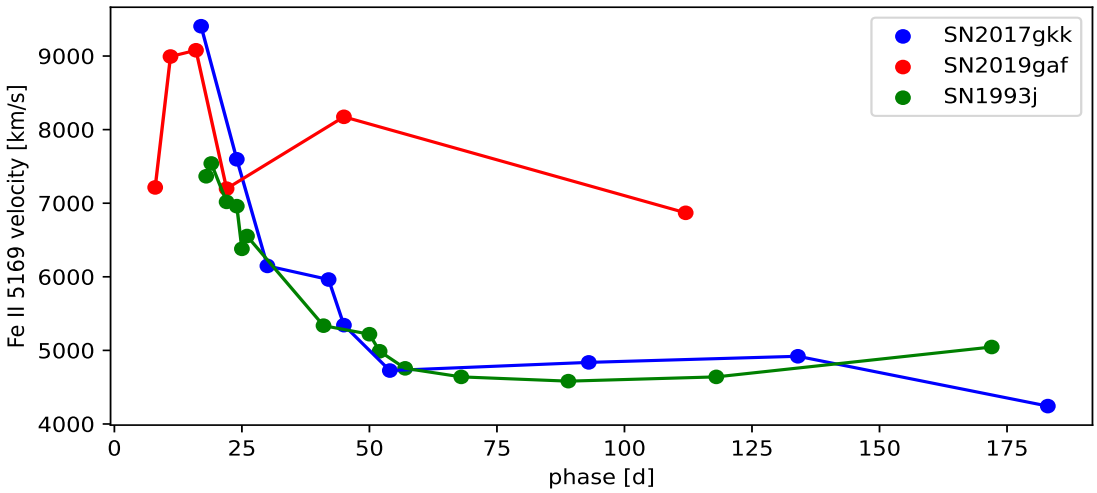

Figure 24. Comparison of velocity evolution of Fe II 5169. Data for SN 1993J were from [42] and for SN 2008ax from [58].

4.6 Explosion date and rise time of SN 2017gkk

The explosion date of SN 2017gkk was estimated using the pseudobolometric LCs of SNe 1993J and 2008ax. Figure **??** shows comparison of bolometric light curves of SNe 1993J, 2008ax and 2017gkk, where peaks are shifted to zero days and scaled to 1. In this figure we can see the similarity of light curves between these SNe, which suggest that rise time of SN 2017gkk is similar with SNe 1993J and 2008ax. In this thesis rise time for SN 2017gkk was assumed to be 20 days, which determines also explosion date to 17.8.2017 (MJD 57982).

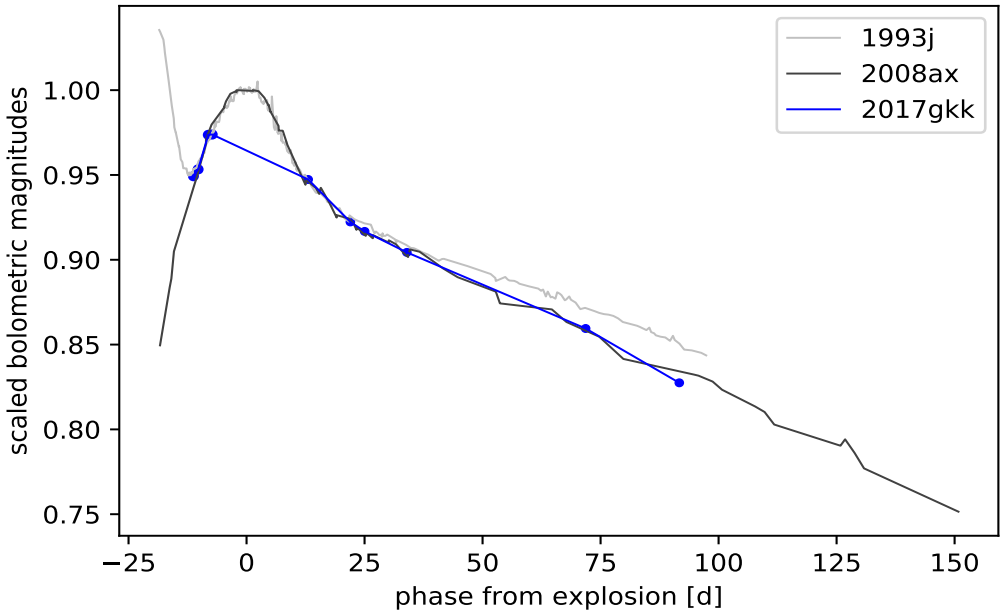

Figure 25. Comparison of pseudobolometric LCs shifted and scaled to same peak date and peak magnitude.

4.7 Explosion date and rise time of SN 2019gaf

The explosion date for SN 2019gaf is assumed to be at the middle point between the latest non-detection date and the discovery date (see fig. 26). Difference between the explosion date and the peak date was 16.73 day, which is assumed to be the rise time in this thesis.

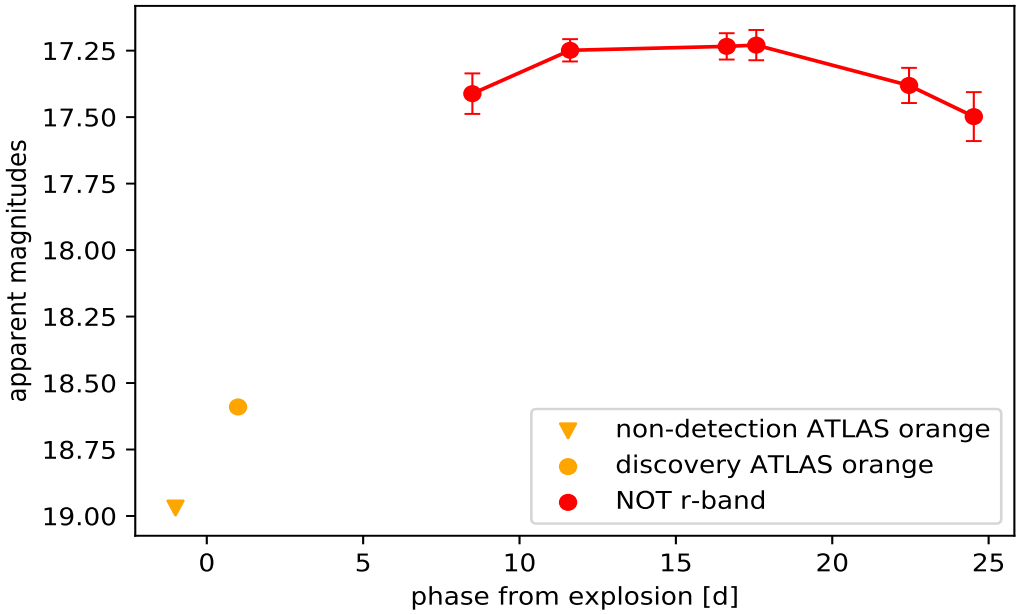

Figure 26. Observations used in the rise time estimation for SN 2019gaf.

5 Discussion

5.1 Nickel mass

The amount of ^{56}Ni in an SN ejecta is an essential factor determining its photospheric evolution. The radioactive decay of ^{56}Co, to which ^{56}Ni decays, is the most important source of energy in nebular phase. In this thesis I estimated M_{Ni56} using Arnett's equation (7) assuming that the bolometric luminosity in the tail phase comes from the radioactivite decay of ^{56}Co. For SN 2017gkk I used the epoch of 123 days after explosion, which gives M_{Ni56} is 0.020 $M_\odot$. For SN 2019gaf I used epoch at 115 days after explosion, which gives M_{Ni56} is 0.073 $M_\odot$. Compared to typical mass of M_{Ni56} for type IIb SNe (0.13 $M_\odot$) [59], SNe 2017gkk and 2019gaf have lower M_{Ni56}.

$$M_{Ni56} = L_R/(6.45 \cdot 10^{43} e^{-t/8.8days} + 1.45 \cdot 10^{43} e^{-t/111.3days}) \quad (7)$$

where L_R is radioactivity luminosity (energy released as γ-rays) in erg/s and M_{Ni56} is mass of radioactive ^{56}Ni in solar masses. 8.8 days is decay constant of ^{56}Ni and 111.3 days decay constant of ^{56}Co. [15]

5.2 Rise time and ejecta mass

The rise time was measured as the time from the explosion to the luminosity peak. Once a SN occurs, the SN ejecta are expanding and the optical depth of the ejecta is decreasing with time. The luminosity of the SN at any moment is determined by the number of photons that could escape from the ejecta at that moment. The diffusion time, t_d, is the average time of photons to escape from the ejecta. The dynamical time of the SN ejecta is defined as the ratio of the radius of the ejecta to the ejecta velocity. The peak luminosity is achieved when these timescales are equal.

The diffusion time depends on the optical depth, which depends on the opacity and the density of the ejecta, as described in equation 8.

$$t_d = \frac{\kappa M}{\beta c R} \tag{8}$$

where κ is the opacity, M is ejecta mass, β is a constant of integration that value is 13.8, c is speed of light and R is radius of ejecta. I assumed the opacity as 0.1 cm^2 g^{-1}, which is a typical values for ionized gas.[15] From the diffusion and dynamical time, the density of the ejecta at the luminosity peak can be calculated. Using the rise time and the velocity of the photosphere, a typical size of the ejecta can be estimated and thus the ejecta mass with this equation:

$$M_{ej} \approx M_{diff} = \frac{1}{2}\frac{\beta c}{\kappa} v_{ph} t_{max}^2 \tag{9}$$

where v_{ph} is velocity of photosphere and t_{max} is rise time. This equation only considers those components, which contributes to the opacity. If the ejecta has

nonionized gas, which has low opacity, the ejecta mass estimated this way is too low. [15]

The photospheric velocity is assumed to be the velocity that is derived from the Fe II absorption minimum at the luminosity peak. The derived velocities for SNe 2019gaf and 2017gkk are 9100 km/s and 7600 km/s, respectively.

SN 2019gaf rise time 16.73 days is clearly shorter than those of other type IIb SNe (see fig 21) and rise time for SN 2017gkk is more typical 20 days. The estimated ejecta masses for SNe 2017gkk and 2019gaf are 2.36 $M_\odot$ and 1.97 $M_\odot$, respectively.

5.3 Kinetic energy of ejecta

$$E_k = \frac{3}{20} \cdot \frac{\beta c}{\kappa} v_{ph}^3 t_{max}^2 \tag{10}$$

This estimation assumes that the mean expansion velocity is 3/5 from the photospheric velocity. Using this with equation 9 the kinetic energy is estimated for SNe 2017gkk and 2019gaf 8.12 $\cdot 10^{50} erg$ and 9.67 $\cdot 10^{50} erg$, respectively. [15]

5.4 Progenitor mass of SNe 2017gkk and 2019gaf

The ratio of the forbidden emission lines, [Ca II]$\lambda 7291, 7323$ and [O I] $\lambda 6300, 6364$, in a nebular spectrum of a SN can be used to estimate the mass of its progenitor. The [O I] line becomes stronger as the progenitor mass increases, because the oxygen burning depends strongly on the progenitor mass, compared to the [Ca II] line which strength increase weakly as the progenitor mass increases.[60]

In this thesis I estimated the progenitor masses of SNe 2017gkk and 2019gaf by comparing the [Ca II]/[O I]/ ratio in their nebular spectra to the theoretical calculations from [61]. Comparisons are presented in fig. 27 and fig. 28 which gives limits to the helium star (helium and heavier elements) masses of these SNe. For SN 2017gkk, the [Ca II]/[O I] ratio suggests helium star mass of 6-7 $M_\odot$ which would correspond to 23-26 $M_\odot$ as its ZAMS mass. For SN 2019gaf, the [Ca II]/[O I] ratio

suggests that helium star mass of 8-12 $M_{\odot}$ which would correspond to 28-36 $M_{\odot}$ as its ZAMS mass. Here I assumed the results of the stellar evolution calculations from [62].

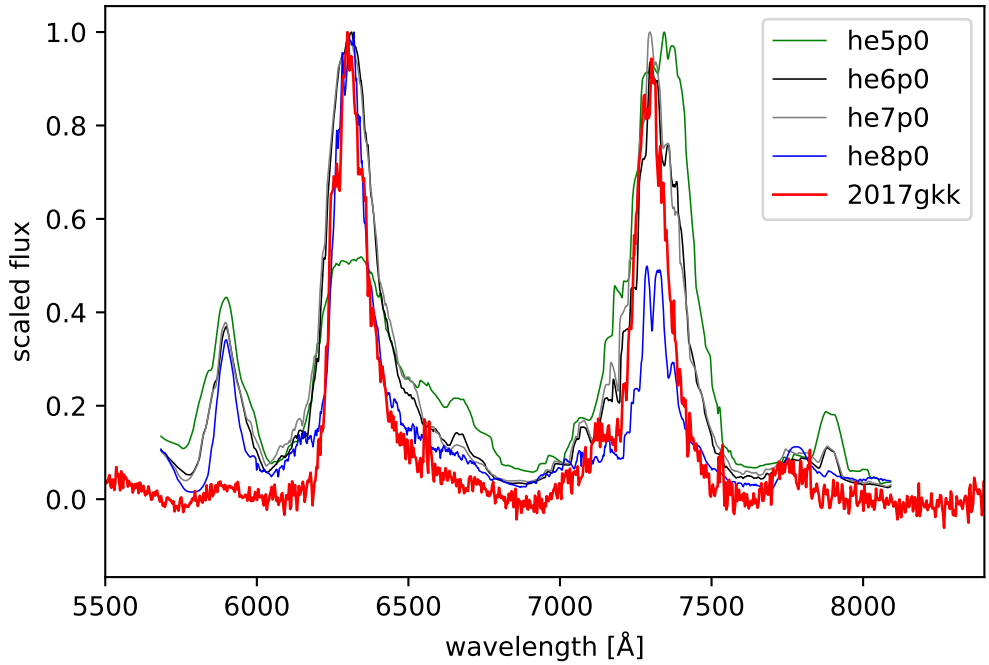

Figure 27. Comparison of models he5p0, he6p0, he7p0 and he8p0 with latest (174 days after explosion) spectrum of SN 2017gkk. Models corresponds to helium star mass. For example he8p0 corresponds to 8.0 $M_{\odot}$. [61]

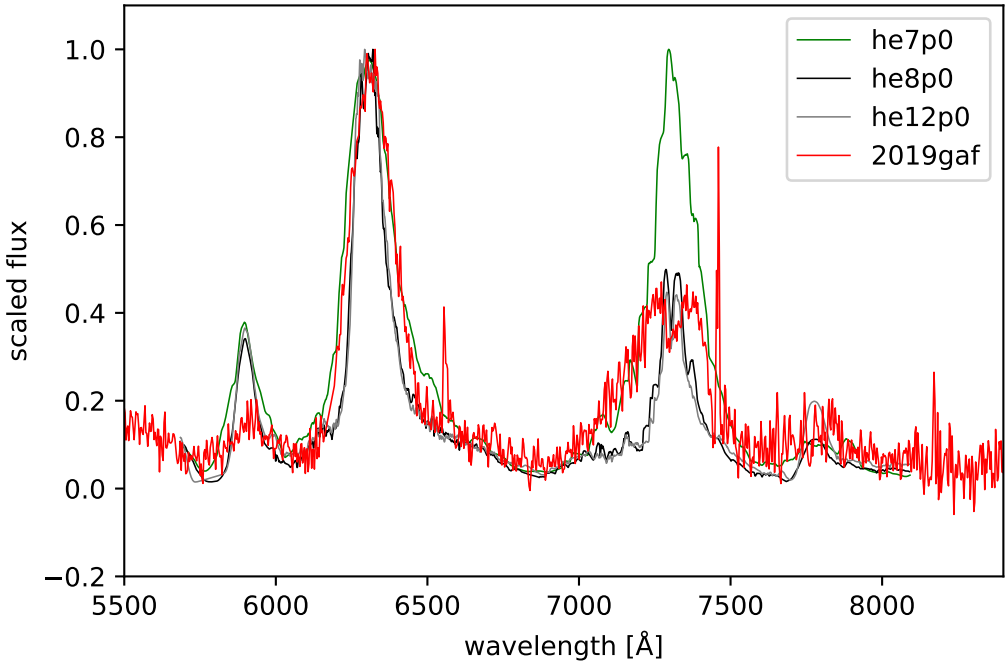

Figure 28. Comparison of models he7p0, he8p0 and he12p0 with latest (203 days after explosion) spectrum of SN 2019gaf.[61]

6 Conclusions

In this thesis I studied two type IIb SNe 2017gkk and 2019gaf using both photometric and spectroscopic observations. The purpose of this thesis is to understand the properties of the type IIb progenitors, which could be used to study the mechanisms for their mass loss.

The photometric results (4.2) are used to construct the pseudobolometric light curve and the color evolution. Then, I compared them to well studied type IIb SNe 1993J and 2008ax. The light curves are used to estimate the ^{56}Ni mass and the rise times. The spectroscopic results (4.1) are used to measure the line velocities for Hα, He I and Fe II. The latest spectra are used to estimate the progenitor masses based on the [Ca II]/[O I] ratio.

In the results following properties for SNe 2017gkk and 2019gaf are derived: the ejecta masses 2.4 $M_\odot$ and 2.0 $M_\odot$, the expansion velocity of ejecta at the peak 7600 km/s and 9100 km/s and for the M_{Ni56} 0.020 $M_\odot$ and 0.073 $M_\odot$, respectively. The mass estimation of the progenitors of SNe 2017gkk and 2019gaf using the [Ca II]/[O I] ratio suggest that zero age main sequence (ZAMS) masses were over 23 and 28 $M_\odot$, but further analysis is needed to see if this is real.

In conclusion SN 2017gkk is more similar with SNe 1993J and 2008ax, than SN 2019gaf, in the rise time and the ^{56}Ni mass. For better analysis it would be useful to have more photometric observations from early phases to constrain more accurately rising time and therefore ejecta parameters like expansion velocity and ejecta mass.

In the future these obtained results would need more study. In order to understand the mass loss mechanisms it would be important to have reliable and accurate progenitor mass estimations, because some of the mass loss mechanisms are sensitive to progenitor mass. It is also important to compare these values to larger sample of type IIb SNe and other CCSNe.

Acknowledgements

I would like to thank my supervisors Hanindyo Kuncarayakti, Takashi Nagao and Seppo Mattila, who have helped me more than I could have ever asked. I am also thankful for the support from Claudia Gutiérrez, Thomas Reynolds and other members of UTU transient group. Lastly, I would like to thank my family for all the support, which has made this thesis possible.

References

[1] W. Baade and F. Zwicky, Proceedings of the National Academy of Science **20**, 254 (1934).

[2] P. Podsiadlowski, in *Handbook of Supernovae*, edited by A. W. Alsabti and P. Murdin (Springer International Publishing Cham, 2017), pp. 635–648.

[3] C. Fremling *et al.*, The Astrophysical Journal **895**, 32 (2020).

[4] D. A. Perley *et al.*, The Astrophysical Journal **904**, 35 (2020).

[5] J. L. Tonry *et al.*, Publications of the Astronomical Society of the Pacific **130**, 064505 (2018).

[6] K. C. Chambers *et al.*, arXiv e-prints arXiv:1612.05560 (2016).

[7] Ž. Ivezić *et al.*, The Astrophysical Journal **873**, 111 (2019).

[8] M. M. Phillips, The Astrophysical Journal **413**, L105 (1993).

[9] K. Maguire, in *Handbook of Supernovae*, edited by A. W. Alsabti and P. Murdin (Springer International Publishing Cham, 2017), pp. 293–316.

[10] D. Richardson *et al.*, The Astronomical Journal **123**, 745 (2002).

[11] L. Zampieri, in *Handbook of Supernovae*, edited by A. W. Alsabti and P. Murdin (Springer International Publishing Cham, 2017), pp. 737–768.

[12] A. V. Filippenko, Annual Review of Astronomy and Astrophysics (1997).

[13] M. Modjaz *et al.*, The Astronomical Journal **147**, 99 (2014).

[14] A. Gal-Yam, in *Handbook of Supernovae*, edited by A. W. Alsabti and P. Murdin (Springer International Publishing Cham, 2017), pp. 195–237.

[15] J. C. W. David Branch, *Supernova Explosions* (Springer Berlin, Heidelberg , 2017).

[16] T. Nagao, Ph.D. thesis, Kyoto University, 2019.

[17] M. Ergon, Ph.D. thesis, Stockholm University, 2015.

[18] E. Pian and P. A. Mazzali, in *Handbook of Supernovae*, edited by A. W. Alsabti and P. Murdin (Springer International Publishing Cham, 2017), pp. 277–292.

[19] I. Arcavi, in *Handbook of Supernovae*, edited by A. W. Alsabti and P. Murdin (Springer International Publishing Cham, 2017), pp. 239–276.

[20] J. Puls, J. S. Vink, and F. Najarro, The Astronomy and Astrophysics Review **16**, 209 (2008).

[21] N. Smith, Annual Review of Astronomy and Astrophysics **52**, 487 (2014).

[22] A. Gilkis and I. Arcavi, Monthly Notices of the Royal Astronomical Society **511**, 691 (2022).

[23] K. I. Nomoto, K. Iwamoto, and T. Suzuki, Physics Reports **256**, 173 (1995).

[24] K. Itagaki, Transient Name Server Discovery Report **2017-940**, 1 (2017).

[25] S. Mattila *et al.*, The Astronomer's Telegram **8992**, 1 (2016).

[26] F. Onori, Transient Name Server Classification Report **2017-964**, 1 (2017).

[27] R. B. Tully, H. M. Courtois, and J. G. Sorce, The Astronomical Journal **152**, 50 (2016).

[28] D. J. Schlegel, D. P. Finkbeiner, and M. Davis, The Astrophysical Journal **500**, 525 (1998).

[29] J. Tonry *et al.*, Transient Name Server Discovery Report **2019-862**, 1 (2019).

[30] E. Swann *et al.*, Transient Name Server Classification Report **2019-902**, 1 (2019).

[31] E. L. Wright, Publications of the Astronomical Society of the Pacific **118**, 1711 (2006).

[32] D. Brout *et al.*, The Astrophysical Journal **938**, 110 (2022).

[33] C. L. Bennett, D. Larson, J. L. Weiland, and G. Hinshaw, The Astrophysical Journal **794**, 135 (2014).

[34] E. F. Schlafly and D. P. Finkbeiner, The Astrophysical Journal **737**, 103 (2011).

[35] Paturel, G. *et al.*, Astronomy and Astrophysics **412**, 45 (2003).

[36] D. Tody, in *Instrumentation in astronomy VI*, Vol. 627 of *Society of Photo-Optical Instrumentation Engineers (SPIE) Conference Series*, edited by D. L. Crawford (Society of Photo-Optical Instrumentation Engineers , 1986), p. 733.

[37] E. Cappellaro, foscgui is a graphic user interface aimed at extracting SN spectroscopy and photometry obtained with FOSC-like instruments. It was developed by E. Cappellaro. A package description can be found at http://graspa.oapd.inaf.it/foscgui.html.

[38] S. J. Brennan and M. Fraser, Astronomy & Astrophysics **667**, A62 (2022).

[39] K. Nilsson, in *Havaitseva tähtitiede*, *Ursan julkaisuja*, 3. laitoksen 1. p. ed., edited by K. Nilsson, L. Takalo, and . Piironen, Jukka (Tähtitieteellinen yhdistys Ursa Helsinki, 2006), 3. laitoksen 2. p. 2009. - 3. laitoksen 3. p. 2011.

[40] A. A. Henden *et al.*, in *American Astronomical Society Meeting Abstracts #232*, Vol. 232 of *American Astronomical Society Meeting Abstracts* (American Astronomical Society , 2018), p. 223.06.

[41] J. Guillochon, J. Parrent, L. Z. Kelley, and R. Margutti, The Astrophysical Journal **835**, 64 (2017).

[42] R. Barbon *et al.*, Astronomy and Astrophysics Supplement **110**, 513 (1995).

[43] M. W. Richmond, R. R. Treffers, A. V. Filippenko, and Y. Paik, The Astronomical Journal **112**, 732 (1996).

[44] M. W. Richmond *et al.*, The Astronomical Journal **107**, 1022 (1994).

[45] P. J. Benson *et al.*, The Astronomical Journal **107**, 1453 (1994).

[46] W. van Driel *et al.*, Publications of the Astronomical Society of Japan **45**, L59 (1993).

[47] M. Okyudo *et al.*, Publications of the Astronomical Society of Japan **45**, L63 (1993).

[48] N. V. Metlova *et al.*, Astronomy Letters **21**, 598 (1995).

[49] H. Mikuz, B. Dintinjana, and T. Zwitter, International Astronomical Union Circulars **5796**, 2 (1993).

[50] X. Zhou, International Astronomical Union Circulars **5782**, 2 (1993).

[51] D. Y. Tsvetkov *et al.*, Peremennye Zvezdy **29**, 2 (2009).

[52] P. J. Brown *et al.*, Astrophysics and Space Science **354**, 89 (2014).

[53] A. Pastorello *et al.*, Monthly Notices of the Royal Astronomical Society **389**, 955 (2008).

[54] M. S. Bessell, F. Castelli, and B. Plez, Astronomy and Astrophysics, **333**, 231 (1998).

[55] T. Matheson *et al.*, The Astronomical Journal **120**, 1499 (2000).

[56] J. A. Cardelli, G. C. Clayton, and J. S. Mathis, The Astrophysical Journal **345**, 245 (1989).

[57] J. Vinko, K. Sarneczky, O. Hanyecz, and A. Sodor, The Astronomer's Telegram **10686**, 1 (2017).

[58] R. Chornock *et al.*, The Astrophysical Journal **739**, 41 (2011).

[59] N. Afsariardchi *et al.*, The Astrophysical Journal **918**, 89 (2021).

[60] A. Jerkstrand *et al.*, Astronomy & Astrophysics **573**, A12 (2015).

[61] L. Dessart *et al.*, Astronomy Astrophysics **656**, A61 (2021).

[62] T. Ertl, S. E. Woosley, T. Sukhbold, and H. T. Janka, The Astrophysical Journal **890**, 51 (2020).